# The Walker circulation, diabatic heating, and outgoing longwave radiation

Samuel N. Stechmann[1,2] and H. Reed Ogrosky[1]

Submitted on June 26, 2014
Revised on September 2, 2014
Revised on October 17, 2014

For the tropical atmosphere on planetary scales, it is common to model the circulation using strong damping. Here, with new data analysis techniques, evidence suggests that damping can actually be neglected. Specifically, near the equator, the east–west overturning circulation is in agreement with the undamped wave response to atmospheric heating. To estimate the heating, satellite observations of outgoing longwave radiation (OLR) are used. Frequently OLR is used as a heuristic indicator of cloudiness. Here, the results further suggest that OLR variations are actually proportional to diabatic heating variations, with a proportionality constant of 18 W $m^{-2}$ (K $day^{-1})^{-1}$. While the agreement holds best over long time averages of years or decades, it also holds over shorter periods of one season or one month. Consequently, it is suggested that the strength of the Walker circulation—and its evolution in time—could be estimated using satellite data.

## 1. Introduction

Two overturning circulations exist in the tropical atmosphere. In the north–south direction is the Hadley circulation, and in the east–west direction is the Walker circulation. The overturning is coupled with cloud patterns and precipitation: ascending air occurs in regions of deep convection, and descending air is correlated with desert regions. For the Walker circulation, this is illustrated schematically in Fig. 1a. While the Walker circulation is traditionally defined as only the circulation cell over the Pacific Ocean [*Bjerknes*, 1969], here the term will sometimes be used more broadly to include all east–west overturning circulations in the Tropics, of which the Pacific cell is one of the strongest. As such a strong component of the climate system, the Walker circulation has global significance and is intimately tied to monsoons, the El Niño–Southern Oscillation (ENSO) [*Julian and Chervin*, 1978], and associated biogeochemical processes [*Barber and Chavez*, 1983].

It is common to model the Walker circulation using strong damping. The most likely candidates for this damping are momentum damping through convective momentum transport and temperature damping through radiative cooling. In mathematical form, these processes are typically represented as Rayleigh friction, $-u/\tau_u$, and Newtonian cooling, $-\theta/\tau_\theta$, respectively, where $u$ is the east–west velocity and $\theta$ is the potential temperature. Such damping is a staple of tropical climate modeling; it is in standard use for not only the Walker circulation [*Matsuno*, 1966; *Webster*, 1972; *Gill*, 1980; *Gill and Rasmusson*, 1983; *Heckley and Gill*, 1984] but also monsoonal circulations [*Webster*, 1972; *Gill*, 1980], the El Niño–Southern Oscillation [*Gill and Rasmusson*, 1983; *Zebiak and Cane*, 1987], and the Madden–Julian oscillation [*Chao*, 1987; *Biello and Majda*, 2005]. Estimates of the damping time scales $\tau_u$ and $\tau_\theta$ are typically in the range of 1–10 days, a strong damping for climatological phenomena that are usually measured with monthly, seasonal, or yearly averages.

It has been noted by several studies that the need for strong damping seems unsettling [*Neelin*, 1988; *Battisti et al.*, 1999]. On the other hand, some studies have also offered justifications. For example, *Holton and Colton* [1972] found that a strong damping is needed in their model to obtain agreement with the observed vorticity field at 200 hPa. They furthermore conjecture that convective momentum transport is the mechanism responsible for the strong damping. Along these lines, *Lin et al.* [2008] also present evidence for strong damping and suggest that the damping rate is spatially inhomogeneous.

Another issue in modeling the Walker circulation is the specification of diabatic heating. Obtaining accurate estimates of diabatic heating is an ongoing challenge and is discussed in more detail below.

The purpose of this paper is to apply a new data analysis procedure to investigate the observed Walker circulation, and to compare it with a simple model. The evidence from this investigation will suggest two surprising results: (i) the Walker circulation can be modeled without damping, and (ii) outgoing longwave radiation (OLR) variations are not only a heuristic indicator of cloudiness but are actually proportional to diabatic heating variations.

## 2. Data, Methods, and Model

### 2.1. Data

Two data sources are used here. First, as a surrogate for atmospheric heating, NOAA interpolated outgoing longwave radiation (OLR) is used [*Liebmann and Smith*, 1996]. Second, NCEP/NCAR reanalysis data is used for all other variables: wind, geopotential height, and sea surface temperature [*Kalnay et al.*, 1996]. Both datasets have a horizontal spatial resolution of $2.5^\circ \times 2.5^\circ$ and a daily temporal resolution from 1 January 1979 to 31 December 2011.

### 2.2. Methods

In this section, a procedure is described to identify Kelvin and equatorial Rossby wave amplitudes from observational data. These waves are commonly used to describe the structure of the Walker circulation [*Gill*, 1980]. To identify their

[1]Department of Mathematics, University of Wisconsin, Madison, Wisconsin, USA.
[2]Department of Atmospheric and Oceanic Sciences, University of Wisconsin, Madison, Wisconsin, USA.


0094-8276/14/$5.00

amplitudes $K(x)$ and $R_m(x)$ ($m = 1, 2, 3, \cdots$) from observational data, a procedure was recently introduced and described in detail elsewhere [*Stechmann and Majda*, 2014]. Here an overview of the procedure is described for the present focus on the Walker circulation, as opposed to the procedure's original focus of the Madden–Julian oscillation, which requires additional steps beyond what is needed here. Here, the method involves two steps: a vertical mode truncation to move from 3D $(x, y, z)$ to 2D $(x, y)$, and then a meridional mode truncation to move to 1D $(x)$.

The first step distinguishes the overturning component of tropical circulations, which is characterized by opposing zonal winds in the lower troposphere (850 hPa) and upper troposphere (200 hPa), as indicated in the schematic diagram in Fig. 1a. To define these first baroclinic mode variables, a simple method is used here. The method utilizes data from only two pressure levels, 850 and 200 hPa, in order to capture the essence of the first baroclinic mode structure:

$$u(x,y) = \frac{\mathrm{U850}(x,y) - \mathrm{U200}(x,y)}{2\sqrt{2}} \quad (1)$$

$$v(x,y) = \frac{\mathrm{V850}(x,y) - \mathrm{V200}(x,y)}{2\sqrt{2}} \quad (2)$$

$$\theta(x,y) = -\frac{\mathrm{Z850}(x,y) - \mathrm{Z200}(x,y)}{2\sqrt{2}} \quad (3)$$

where $Z$ is geopotential height and is related to potential temperature anomaly $\theta$ via a hydrostatic balance equation. (The equations have been nondimensionalized using standard equatorial reference scales [*Stechmann et al.*, 2008; *Majda and Stechmann*, 2009; *Stechmann and Majda*, 2014], which result in an equivalent depth of roughly 260 m and a gravity wave speed of roughly 50 m/s.) In Eqs. 1–3, by taking the difference between the data at 850 and 200 hPa, this method isolates the overturning component of tropical circulations from the barotropic component.

In the second step, the method furthermore breaks down the overturning circulation into its individual wave components, such as the Kelvin wave amplitude $K(x)$ and the long-wave equatorial Rossby wave amplitudes $R_m(x)$. To accomplish this, meridional basis functions $\phi_m(y)$ are used to write the expansion $u(x,y) = \sum_{m=0}^{\infty} u_m(x)\,\phi_m(y)$, where the functions $\phi_m(y)$ are the parabolic cylinder functions, and where the quantities $u_m(x)$ are obtained using the projections $u_m(x) = \int_{-\infty}^{\infty} u(x,y)\phi_m(y)\,dy$. Similar formulas also apply for $\theta(x,y)$ and $\theta_m(x)$. Utilizing these projections, the wave amplitudes $K(x)$ and $R_m(x)$ are defined as

$$K(x) = \frac{1}{\sqrt{2}}(u_0 - \theta_0) \quad (4)$$

$$R_m(x) = \frac{\sqrt{m+1}}{\sqrt{2}}(u_{m+1} - \theta_{m+1}) - \frac{\sqrt{m}}{\sqrt{2}}(u_{m-1} + \theta_{m-1}), \quad m = 1, 2, 3, \cdots \quad (5)$$

More details are provided in the auxiliary materials or by *Stechmann and Majda* [2014].

### 2.3. Model

For comparison with the observed Kelvin and Rossby wave amplitudes ($K(x)$ and $R_m(x)$), a simple model is used to predict these wave amplitudes, given heat and momentum forcing functions. The model is similar to the classical Matsuno–Gill model [*Matsuno*, 1966; *Gill*, 1980], except no damping is used here. Contemporary derivations formulate the model explicitly in terms of the $K(x)$ and $R_m(x)$ variables [*Biello and Majda*, 2006; *Majda and Stechmann*, 2009; *Stechmann and Majda*, 2014]; the model equations for these variables are described below. Also, heat and momentum sources must be specified as inputs to the model, as described below. See the auxiliary materials for more details.

## 3. Results and Discussion

### 3.1. Stationary Kelvin wave

The Walker circulation can be viewed as a stationary wave pattern. Figure 1b,c illustrates the first component of this pattern, the Kelvin wave. Its amplitude is strongest near the equator and decays as $\exp[-y^2/(2L_E^2)]$ where $L_E$ is an equatorial trapping scale of roughly 1500 km, or 13.5° latitude. To obtain the observed wave pattern, zonal wind and geopotential height data have been projected onto the theoretical structure of the Kelvin wave, using its vertical ($z$) and meridional ($y$) structure [*Majda and Stechmann*, 2009; *Stechmann and Majda*, 2014].

To compare with the observed Kelvin wave in Fig. 1b, a linear model predicts the Kelvin wave amplitude shown in Fig. 1c. The model prediction agrees with observations with a pattern correlation of 0.98.

To predict the amplitude $K(x)$ of the stationary Kelvin wave, the following model is used:

$$\frac{dK}{dx} = -\frac{1}{\sqrt{2}}(F_{\mathrm{heat}} - F_{\mathrm{mom}}), \quad (6)$$

where $F_{\mathrm{heat}}$ is the atmospheric heating rate and $F_{\mathrm{mom}}$ is the atmospheric momentum forcing, appropriately nondimensionalized. This agreement in Fig. 1 is surprising, since the Kelvin wave model in Eq. 6 is an undamped model [*Majda and Stechmann*, 2009; *Stechmann and Majda*, 2014], whereas previous model results used a strong damping with time scale of 1–10 days [*Matsuno*, 1966; *Webster*, 1972; *Gill*, 1980; *Gill and Rasmusson*, 1983; *Heckley and Gill*, 1984; *Zebiak and Cane*, 1987; *Chao*, 1987; *Biello and Majda*, 2005].

The effect of damping is illustrated in the auxiliary materials. If 1-day damping is included, a significant phase error is introduced, and the pattern correlation in Fig. 1c would be reduced to 0.82. On the other hand, if 5-day damping is included, the result is similar to Fig. 1c, and the pattern correlation is 0.97. This suggests that the model result is essentially the same for any damping with a time scale of 5 days or longer, including the preferred choice here of neglecting the damping altogether.

Since undamped waves will continue to oscillate and propagate without decay, the concept of a steady undamped wave pattern merits some consideration. The steady undamped model in Eq. 6 could be interpreted in two ways. One interpretation is that it is a temporal average of the unsteady equation for Kelvin waves. In this case, through the temporal average, the influence of propagating Kelvin waves is averaged out, leaving only the steady Kelvin wave pattern described by Eq. 6. Another interpretation is that Eq. 6 describes the steady state that would be achieved in a damped model, in the limit that the damping rate tends to zero. This is a regular limit in the setup used here, although in other cases the limit can potentially be subtle, since certain consistency conditions must be satisfied by the forcing in the undamped limit, as pointed out by *Majda and Klein* [2003]. See the auxiliary materials for further discussion.

What is different about the approach here compared to previous studies? How are pattern correlations of 0.98 achieved here without damping, whereas previous studies reported a need for strong damping? Several aspects here are notable, such as: (i) the zonal mean component is not

considered, (ii) the first baroclinic mode is isolated by a new observational analysis technique, and (iii) accurate estimates of diabatic heating variations, $F_{\text{heat}}$, and momentum forcing, $F_{\text{mom}}$, must be input to the model in Eq. 6. Further discussion is provided in the subsequent sections, and some subtle points are described in detail in the auxiliary materials.

### 3.2. Diabatic heating and outgoing longwave radiation

To model the Walker circulation as a steady wave response as in Eq. 6 and Fig. 1, one must know the atmospheric momentum sources ($F_{\text{mom}}$) and heat sources ($F_{\text{heat}}$) that shape the circulation. These sources have proven difficult to measure from observational data. The two most important heat sources are arguably (i) latent heating, which occurs within clouds, due to the phase change of water vapor to condensed water, and (ii) radiative cooling. For both of these heat sources, extensive programs have been created to retrieve estimates from satellite data [*Ramanathan et al.*, 1989; *Rossow and Lacis*, 1990; *Tao et al.*, 2006; *L'Ecuyer and McGarragh*, 2010]. The retrieval algorithms are quite complex, and they incorporate a variety of satellite-observed data. Assessing the accuracy of these methods is a major ongoing challenge.

One relatively simple quantity measured from satellites is outgoing longwave radiation (OLR). OLR is the total power per unit area (W m$^{-2}$) of electromagnetic radiation emitted to space by the Earth–atmosphere system.

The Earth and atmosphere both emit radiation that contributes to OLR, and hence raw OLR data is not widely used by itself as an estimate of atmospheric radiative cooling. Moreover, the Earth-emitted portion and atmosphere-emitted portion cannot be easily separated, partly because Earth-emitted radiation is affected by the atmosphere on its way to space. For instance, it is partially absorbed by atmospheric constituents such as carbon dioxide, water vapor, and liquid water and ice in clouds. Consequently, unless additional information is known about the atmospheric state, it appears difficult to use OLR data to isolate atmospheric radiative heating.

Since clouds affect OLR, it is natural to use OLR data as an indicator of cloudiness in the tropics [*Gruber*, 1974; *Zangvil*, 1975; *Knutson and Weickmann*, 1987; *Wheeler and Kiladis*, 1999; *Wheeler and Hendon*, 2004]. Based on black-body radiation theory, it is expected that a negative anomaly of OLR should indicate a cloudy region, since the temperature at cloud top is lower than at the Earth's surface. Following this expectation, statistical correlations have been examined between OLR and upper-tropospheric divergence [*Julian*, 1984], and some satellite rainfall retrieval algorithms make use of OLR or infrared radiances to infer rainfall at the Earth's surface [*Xie and Arkin*, 1997; *Joyce et al.*, 2004]. Furthermore, some studies have examined statistical correlations between OLR and cloud heating [*Christy*, 1991; *Yanai and Tomita*, 1998], although no universal relationship is currently in widespread use. In short, raw OLR data is typically interpreted as a heuristic indicator or proxy of cloudiness, rather than a quantitative measure of a specific cloud property.

Surprisingly, the results in Fig. 1 suggest that OLR is directly related to the total diabatic heating, from all sources, as

$$F_{\text{heat}} = -H_{\text{OLR}} \cdot \text{OLR}, \tag{7}$$

where $F_{\text{heat}}$ and OLR are understood to represent anomalies from the zonal mean. The proportionality constant that provides the best observations-versus-model agreement in Fig. 1c is

$$H_{\text{OLR}} = 0.056 \text{ K d}^{-1} \text{ (W m}^{-2})^{-1}. \tag{8}$$

To obtain the model result in Fig. 1c, it is assumed that the momentum sources are small ($F_{\text{mom}} \approx 0$) compared to the heat sources, and Eqs. 6 and 7 are combined to yield

$$\frac{dK}{dx} = \frac{H_{\text{OLR}}}{\sqrt{2}} \cdot \text{OLR}, \tag{9}$$

which predicts that the Kelvin wave amplitude can be inferred from the integral of the satellite OLR variations.

Relationships such as Eq. 7 can be difficult to establish accurately; this is because it would require an accurate, independent measure of diabatic heating, $F_{\text{heat}}$, which is a major ongoing challenge [*Ramanathan et al.*, 1989; *Rossow and Lacis*, 1990; *Christy*, 1991; *Yanai and Tomita*, 1998; *Tao et al.*, 2006; *L'Ecuyer and McGarragh*, 2010]. Here, this problem is circumvented by using Eq. 6, which allows Eq. 7 to be inferred by comparing OLR with wind and geopotential height data, which are among the most accurately measured of all atmospheric quantities, a point that lends confidence to Eq. 7.

### 3.3. El Niño, La Niña, and seasonal time scales

While Fig. 1 suggests Eqs. 6–9 are valid in a 30-year average, it is natural to next explore shorter time scales. Figure 2 shows the Kelvin wave averaged over 3-month segments. The two contrasting segments display the El Niño and La Niña phases of the unusually strong El Niño event of 1997–1998 [*McPhaden*, 1999]. In addition to providing tests on shorter time scales, these two segments were also chosen to test the relationships in Eqs. 6–9 across some of the most extreme variations of the Walker circulation. Even in these two extreme cases, the model-predicted, undamped Kelvin wave agrees with the observed Kelvin wave, with pattern correlations of 0.94 and 0.91.

### 3.4. Stationary Rossby waves

The results in Figs. 1 and 2 suggest that the strength of the Walker circulation could be inferred from satellite observations. However, in addition to the Kelvin wave contribution, the total Walker circulation also includes contributions from equatorial Rossby waves.

To assess the model predictions of the Rossby waves, the first Rossby wave pattern $R_1$ is shown in Fig. 3. Thirty-year averages are shown for each of four separate seasons. For three of the seasons, the model skill is comparable to its skill for the Kelvin wave. For the other season, spanning December, January, and February, the modeled Rossby wave is stronger than the observed Rossby wave. Overall, in the annual average, the pattern correlation between observed $R_1$ and (undamped) modeled $R_1$ is 0.98, which is comparable to the Kelvin wave case.

Rossby waves make important contributions to both the equatorial and off-equatorial circulation. Due to the off-equatorial character of the Rossby waves, some of them can become difficult to model with the approach used here. This is due to a multitude of reasons. For instance, equatorial wave theory eventually breaks down away from the equator; and the topographic effects of Tibet and the Andes are influential off-equatorial features that are neglected by idealized wave theories. Also, in the Rossby wave model, north–south velocity $v$ is also incorporated; while $v$ could potentially be predicted from OLR observations and the model, the results here include observed $v$ along with observed OLR to predict the long-wave Rossby pattern $R_m(x)$ via

$$\begin{aligned}\frac{dR_m}{dx} &= (2m+1)v_m + \frac{\sqrt{m+1}}{\sqrt{2}}(f^u_{m+1} - f^\theta_{m+1}) \\ &\quad + \frac{\sqrt{m}}{\sqrt{2}}(f^u_{m-1} + f^\theta_{m-1}), \quad m = 1, 2, 3, \cdots\end{aligned} \tag{10}$$

where the details of this equation are described in the auxiliary materials or by *Stechmann and Majda* [2014]. A further possible complexity with Rossby waves is that the OLR observations are needed in both equatorial and off-equatorial regions, and one might expect the simple relationship in Eq. 7 to break down as one moves away from the equator and into the subtropics, where large meridional temperature gradients, different cloud types, etc. could possibly change the contributing elements to OLR. To assess this, the next equatorial Rossby waves in the hierarchy are examined. In the auxiliary materials, it is shown that $R_2$ is predicted with a pattern correlation of 0.96, nearly as high as the $R_1$ case, but the $R_3$ prediction has a lower pattern correlation of 0.80.

### 3.5. Walker circulation and its Kelvin and Rossby components

Given that the $K$, $R_1$, and $R_2$ waves are predicted well by the model, the next question is: Are the observed $K$, $R_1$, and $R_2$ waves sufficient to capture the main features of the observed Walker circulation? Figure 4 shows the total observed winds and the observed winds obtained from the contributions of the $K$, $R_1$, and $R_2$ waves only. Most features of the total winds are captured by the linear superposition of the $K$, $R_1$, and $R_2$ waves alone, with a pattern correlation of 0.86. In fact, the $K$ and $R_1$ waves alone account for the main broad features of the total observed circulation, with a pattern correlation of 0.80.

## 4. Conclusions

In summary, evidence is presented for two main results: (i) the Walker circulation can be modeled without damping, and (ii) diabatic heating variations are proportional to OLR variations.

Three remarks are in order. First note that the same value $H_{\text{OLR}} = 0.056$ K d$^{-1}$ (W m$^{-2}$)$^{-1}$ has been used for modeling all of the wave types here, which suggests this value is robust. It was calibrated using Eq. 6 for the Kelvin wave case, and one could potentially try to further restrict the calibration to only a single zonal wavenumber such as $k = 1$. Second, note that the zonal mean was removed in establishing the relationship in Eq. 6. As a result, the zonal mean Hadley circulation is not included here. It would be interesting to extend the ideas here to include the zonal mean Hadley circulation, although some initial attempts have not yet been satisfactory. Lastly note that only the overturning (baroclinic) circulation has been considered here, not the barotropic component of the circulation, which is driven by many factors besides diabatic heating alone.

As one application of the methods here, one could potentially estimate the strength of the Walker circulation and its evolution over time. Interesting questions include: Has the Walker circulation been strengthening or weakening? Is there any relationship between the Walker circulation and global climate change [*Vecchi et al.*, 2006; *L'Heureux et al.*, 2013]? Traditionally, Walker circulation strength has been estimated using sea-level pressure, from which one would like to infer the strength of the higher-altitude overturning circulation. In contrast, the methods here quantify the strength of the overturning circulation itself, either from direct measures or from satellite OLR observations. In a preliminary examination of the period 1980–2009, the root-mean-square of the wave patterns $K(x)$ and $R_m(x)$ shows some variations from year to year but no clear long-term trend.

**Acknowledgments.** The data for this paper are available from NOAA/OAR/ESRL PSD, Boulder, Colorado, USA, from their Web site at http://www.esrl.noaa.gov/psd/.

The research of S.N.S. is partially supported by ONR Young Investigator Award N00014-12-1-0744 and by ONR MURI grant N00014-12-1-0912. H.R.O. is supported as a postdoctoral researcher by ONR MURI grant N00014-12-1-0912. The authors thank A. Majda, G. Kiladis, and T. L'Ecuyer for helpful discussion, and T. Dunkerton and an anonymous reviewer for helpful reviews and comments.

## References

Barber, R. T., and F. P. Chavez (1983), Biological consequences of El Niño, *Science*, *222*(4629), 1203–1210.

Battisti, D. S., E. S. Sarachik, and A. C. Hirst (1999), A consistent model for the large-scale steady surface atmospheric circulation in the tropics, *J. Climate*, *12*(10), 2956–2964.

Biello, J. A., and A. J. Majda (2005), A new multiscale model for the Madden–Julian oscillation., *J. Atmos. Sci.*, *62*, 1694–1721.

Biello, J. A., and A. J. Majda (2006), Modulating synoptic scale convective activity and boundary layer dissipation in the IPESD models of the Madden–Julian oscillation, *Dyn. Atmos. Oceans*, *42*, 152–215.

Bjerknes, J. (1969), Atmospheric teleconnections from the equatorial Pacific, *Mon. Wea. Rev.*, *97*(3), 163–172.

Chao, W. C. (1987), On the origin of the tropical intraseasonal oscillation., *J. Atmos. Sci.*, *44*, 1940–1949.

Christy, J. R. (1991), Diabatic heating rate estimates from European Centre for Medium-Range Weather Forecasts analyses, *J. Geophys. Res.*, *96*(D3), 5123–5135.

Gill, A. E. (1980), Some simple solutions for heat-induced tropical circulation, *Q. J. Royal Meteor. Soc.*, *106*(449), 447–462.

Gill, A. E., and E. M. Rasmusson (1983), The 1982-83 climate anomaly in the equatorial pacific, *Nature*, *306*, 229–234.

Gruber, A. (1974), The wavenumber-frequency spectra of satellite-measured brightness in the tropics, *J. Atmos. Sci.*, *31*(6), 1675–1680.

Heckley, W. A., and A. E. Gill (1984), Some simple analytical solutions to the problem of forced equatorial long waves, *Q. J. Royal Meteor. Soc.*, *110*(463), 203–217.

Holton, J. R., and D. E. Colton (1972), A diagnostic study of the vorticity balance at 200 mb in the tropics during the northern summer, *J. Atmos. Sci.*, *29*(6), 1124–1128.

Joyce, R. J., J. E. Janowiak, P. A. Arkin, and P. Xie (2004), CMORPH: A method that produces global precipitation estimates from passive microwave and infrared data at high spatial and temporal resolution, *J. Hydrometeor.*, *5*(3), 487–503.

Julian, P. R. (1984), Objective analysis in the tropics: A proposed scheme, *Mon. Wea. Rev.*, *112*(9), 1752–1767.

Julian, P. R., and R. M. Chervin (1978), A study of the Southern Oscillation and Walker Circulation phenomenon, *Mon. Wea. Rev.*, *106*(10), 1433–1451.

Kalnay, E., M. Kanamitsu, R. Kistler, W. Collins, D. Deaven, L. Gandin, M. Iredell, S. Saha, G. White, J. Woollen, et al. (1996), The NCEP/NCAR 40-year reanalysis project, *Bull. Amer. Meteor. Soc.*, *77*(3), 437–471.

Knutson, T. R., and K. M. Weickmann (1987), 30–60 day atmospheric oscillations: Composite life cycles of convection and circulation anomalies, *Mon. Wea. Rev.*, *115*(7), 1407–1436.

L'Ecuyer, T. S., and G. McGarragh (2010), A 10-year climatology of tropical radiative heating and its vertical structure from TRMM observations., *J. Climate*, *23*(3), 519–541.

L'Heureux, M. L., S. Lee, and B. Lyon (2013), Recent multidecadal strengthening of the Walker circulation across the tropical Pacific, *Nature Climate Change*, *3*(6), 571–576.

Liebmann, B., and C. A. Smith (1996), Description of a complete (interpolated) outgoing longwave radiation dataset, *Bull. Amer. Meteor. Soc.*, *77*, 1275–1277.

Lin, J.-L., B. E. Mapes, and W. Han (2008), What are the sources of mechanical damping in Matsuno–Gill-type models?, *J. Climate*, *21*(2), 165–179.

Majda, A. J., and R. Klein (2003), Systematic multiscale models for the Tropics., *J. Atmos. Sci.*, *60*, 393–408.

Majda, A. J., and S. N. Stechmann (2009), The skeleton of tropical intraseasonal oscillations, *Proc. Natl. Acad. Sci. USA*, *106*(21), 8417–8422.

Matsuno, T. (1966), Quasi-geostrophic motions in the equatorial area, *J. Meteor. Soc. Japan*, *44*(1), 25–43.

McPhaden, M. J. (1999), Genesis and evolution of the 1997-98 El Niño, *Science*, *283*(5404), 950–954.

Neelin, J. D. (1988), A simple model for surface stress and low-level flow in the tropical atmosphere driven by prescribed heating, *Q. J. R. Meteorol. Soc.*, *114*(481), 747–770.

Ramanathan, V., R. D. Cess, E. F. Harrison, P. Minnis, B. R. Barkstrom, E. Ahmad, and D. Hartmann (1989), Cloud-radiative forcing and climate: Results from the Earth Radiation Budget Experiment, *Science*, *243*(4887), 57–63.

Rossow, W. B., and A. A. Lacis (1990), Global, seasonal cloud variations from satellite radiance measurements. Part II. Cloud properties and radiative effects, *J. Climate*, *3*(11), 1204–1253.

Stechmann, S. N., and A. J. Majda (2014), Identifying the skeleton of the Madden–Julian oscillation in observational data, *Mon. Wea. Rev.*, p. submitted.

Stechmann, S. N., A. J. Majda, and B. Khouider (2008), Nonlinear dynamics of hydrostatic internal gravity waves, *Theor. Comp. Fluid Dyn.*, *22*, 407–432.

Tao, W.-K., E. A. Smith, R. F. Adler, A. Y. Hou, R. Meneghini, J. Simpson, Z. S. Haddad, T. Iguchi, S. Satoh, R. Kakar, et al. (2006), Retrieval of latent heating from TRMM measurements, *Bull. Amer. Meteor. Soc.*, *87*(11), 1555–1572.

Vecchi, G. A., B. J. Soden, A. T. Wittenberg, I. M. Held, A. Leetmaa, and M. J. Harrison (2006), Weakening of tropical Pacific atmospheric circulation due to anthropogenic forcing, *Nature*, *441*(7089), 73–76.

Webster, P. J. (1972), Response of the tropical atmosphere to local, steady forcing, *Mon. Wea. Rev.*, *100*(7), 518–541.

Wheeler, M., and G. N. Kiladis (1999), Convectively coupled equatorial waves: analysis of clouds and temperature in the wavenumber–frequency domain, *J. Atmos. Sci.*, *56*(3), 374–399.

Wheeler, M. C., and H. H. Hendon (2004), An all-season real-time multivariate MJO index: Development of an index for monitoring and prediction, *Mon. Wea. Rev.*, *132*(8), 1917–1932.

Xie, P., and P. A. Arkin (1997), Global precipitation: A 17-year monthly analysis based on gauge observations, satellite estimates, and numerical model outputs, *Bull. Amer. Meteor. Soc.*, *78*(11), 2539–2558.

Yanai, M., and T. Tomita (1998), Seasonal and interannual variability of atmospheric heat sources and moisture sinks as determined from NCEP-NCAR reanalysis, *J. Climate*, *11*(3), 463–482.

Zangvil, A. (1975), Temporal and spatial behavior of large-scale disturbances in tropical cloudiness deduced from satellite brightness data, *Mon. Wea. Rev.*, *103*(10), 904–920.

Zebiak, S. E., and M. A. Cane (1987), A model El Niño–Southern Oscillation, *Mon. Wea. Rev.*, *115*(10), 2262–2278.

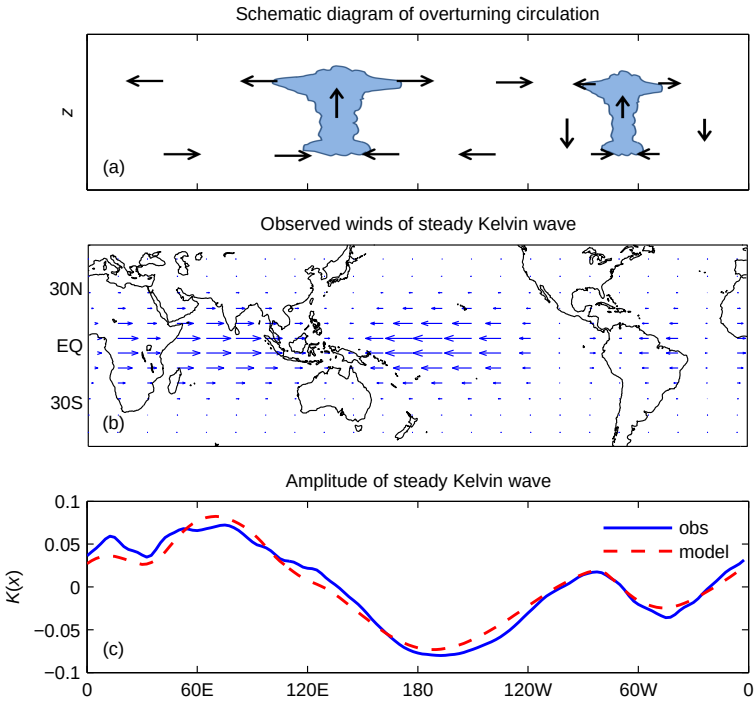


**Figure 1.** (a) Schematic diagram of east–west overturning circulations near the equator. (b) The zonal winds of the Kelvin wave as observed in NCEP/NCAR reanalysis data, averaged from 1980-2009. Displayed is the low-altitude (850 hPa) component of the Kelvin wave's zonal wind. (c) The amplitude of the observed (solid blue line) and model-predicted (dashed red line) Kelvin wave averaged from 1980-2009.

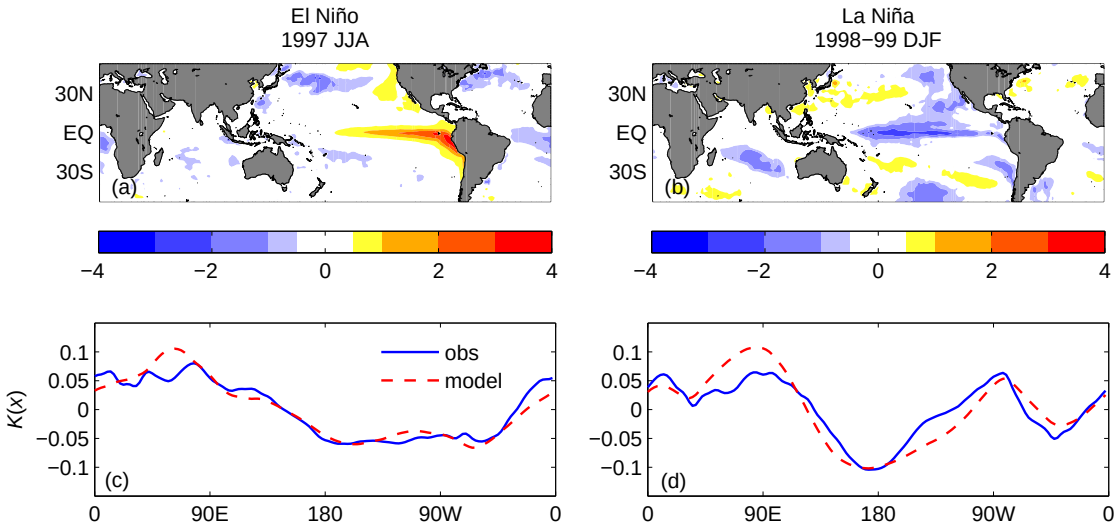


**Figure 2.** The Kelvin wave amplitude during example three-month segments with contrasing ENSO state. Sea surface temperature anomalies (K) are shown for (a) June–July–August of 1997 during a strong El Niño event, and (b) December–January–February of 1998-99 during the subsequent La Niña event. The time-averaged amplitude $K(x)$ of the observed (solid blue line) and model-predicted (dashed red line) Kelvin wave is shown for (c) the 1997 JJA El Niño event, and (d) the 1997-98 DJF La Niña event.

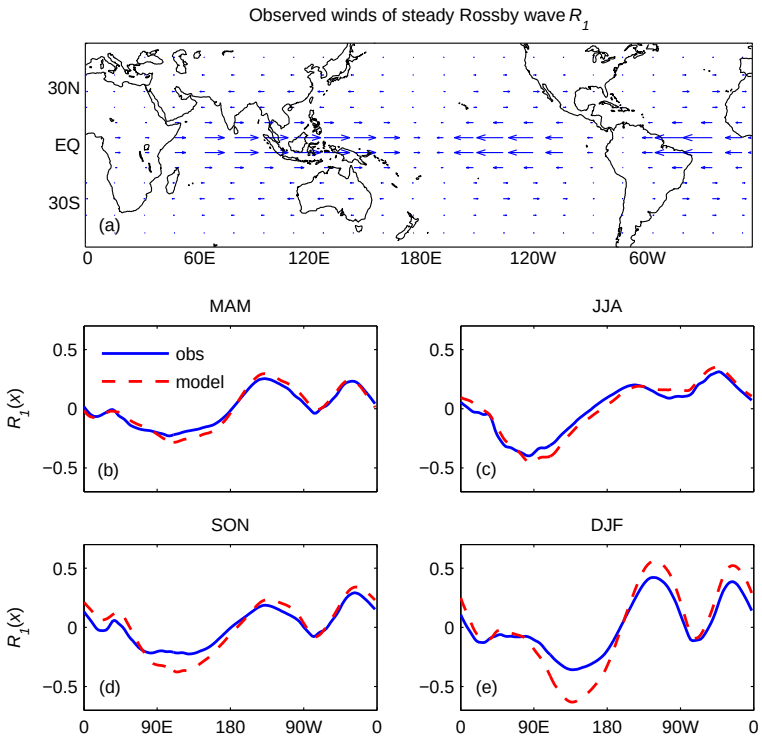


**Figure 3.** (a) The zonal winds of the Rossby wave $R_1$ as observed in NCEP/NCAR reanalysis data, averaged from 1980-2009. The amplitude of the observed (solid blue line) and model-predicted (dashed red line) Rossby wave $R_1$ averaged from 1980-2009 for the (b) MAM, (c) JJA, (d) SON, and (e) DJF seasons.

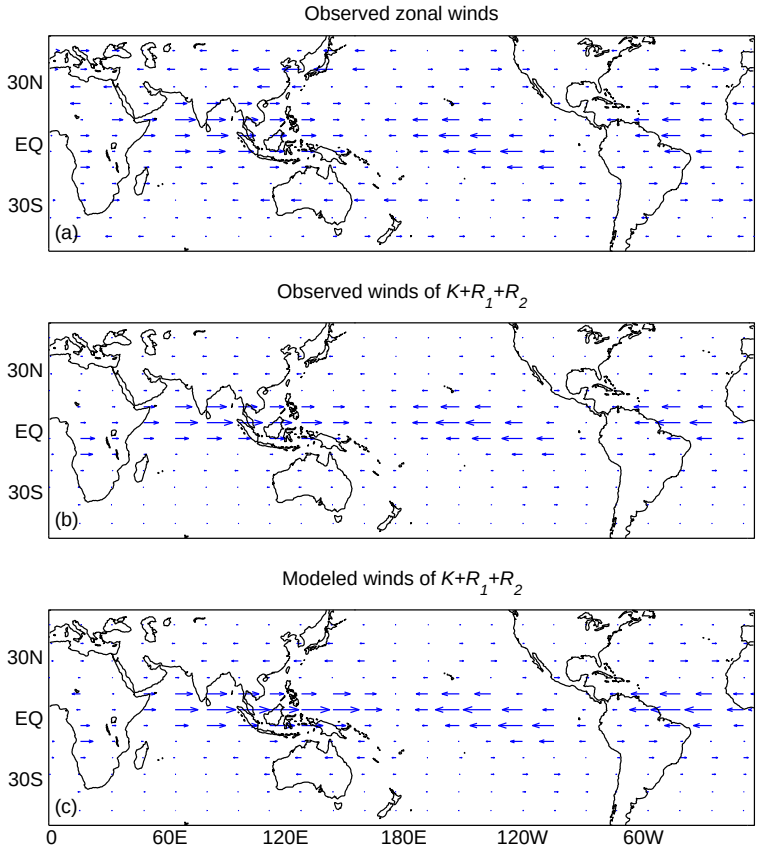


**Figure 4.** (a) Low-altitude (850 hPa) component of zonal winds of the overturning circulation, as observed in NCEP/NCAR reanalysis data, averaged from 1980–2009. (b) Same as (a) except for the wind of only the Kelvin wave $K$ and first two Rossby waves, $R_1$ and $R_2$. (c) Same as (b) except for the model-predicted Kelvin wave $K$ and first two Rossby waves, $R_1$ and $R_2$.